A Biophysical Model for Defibrillation of Cardiac Tissue

James P. Keener* and A. V. Panfilov
*Department of Mathematics, University of Utah, Salt Lake City, Utah 84112 USA and Bioinformatica, Utrecht University, Utrecht, 3584 CH, The Netherlands

ABSTRACT We propose a new model for electrical activity of cardiac tissue that incorporates the effects of cellular microstructure. As such, this model provides insight into the mechanism of direct stimulation and defibrillation of cardiac tissue after injection of large currents. To illustrate the usefulness of the model, numerical stimulations are used to show the difference between successful and unsuccessful defibrillation of large pieces of tissue.

INTRODUCTION

Although defibrillation by the application of large current shocks is accomplished daily in clinics and hospitals around the world, there is no adequate theoretical or experimental explanation for why or how defibrillation works.

There are (at least) two fundamental questions that must be answered. First, how can a spatially localized stimulus have a global effect on the transmembrane potential and thereby affect the activation pattern far from the stimulating electrodes? Second, what are the dynamics of the medium subsequent to the application of a large shock that lead to the elimination of reentrant activation patterns?

A one-dimensional homogeneous excitable bidomain medium cannot be directly activated or defibrillated by the application of a single local stimulus (Plonsey et al., 1991; Krassowska et al., 1987; Keener, 1996). The transmembrane potential dies off exponentially away from the stimulus site, and in the interior no transmembrane current is generated.

There are currently two competing views on how the local confinement of point stimuli can be overcome. One suggestion is that the bidomain nature of cardiac tissue with unequal anisotropy ratios of conductivity leads to activation patterns that are spatially extended beyond those for a bidomain model with equal anisotropy ratios. This view argues for modified patterns of local activation, but not for a global activation from local stimuli, and therefore does not appear to solve the defibrillation dilemma.

A second view is that small-scale inhomogeneities of resistance on the scale of cells induce variations of transmembrane currents, also on the scale of cells, and that these currents can be defibrillating or globally activating if they can be made sufficiently large in amplitude (Keener, 1996; Pumir and Krinsky, 1996). Experimental evidence for this view comes from observations of isolated myocytes in an electrical field wherein the cells were depolarized and hyperpolarized at their opposite ends (Knisely et al., 1993). There is also support for this view from a modeling perspective (Krassowska and Neu, 1994). Opposition to this view comes from the fact that related "sawtooth" variations have not been found in intact cardiac tissue, although they have been sought (Zhou et al., 1995).

The proposal of this paper is that inhomogeneities of resistance are necessary to produce transmembrane current at large distances from the stimulus site. Because transmembrane currents, not intracellular or extracellular fields, are responsible for stimulating the medium, it is important to understand how the resistivities within the extracellular and intracellular domains generate transmembrane currents.

Cardiac tissue exhibits a number of significant nonuniformities. First, cardiac tissue is an anisotropic bidomain. That is, the average resistivities in the directions parallel and transverse to fibers are different and in different ratios for the intracellular and extracellular spaces. Ventricular muscle is a layered three-dimensional tissue. The layers are not planar, and within layers the fiber orientation is variable. Furthermore, there is rotation of fiber orientation between layers.

These variations in fiber structure occur on a spatial scale that is relatively long compared to the space constant of the tissue. In contrast to these long scale variations, resistance to current flow varies rapidly on the spatial scale of cells, primarily because of the gap junctional coupling of cells, but also because of collagen, connective tissue, and layering of myocardial sheets (LeGrice et al., 1995).

When a current is applied to cardiac tissue, the current flow through the tissue responds to all of the resistive variations, and these create transmembrane currents. Thus, end-to-end cellular resistance generates transmembrane current, albeit small, that might stimulate a cell.

In this paper we present a new model for the electrical activity of cardiac tissue that accounts for small-scale variation in resistance (at the level of cells) as well as larger scale tissue variations, such as rotational anisotropy and fiber curvature. As a result of this new feature, this new model admits the possibility of direct activation and defibrillation as well as normal propagation of action potentials, a combination that is not possible in previous models. The

Received for publication 17 January 1996 and in final form 29 May 1996.
Address reprint requests to Dr. James P. Keener, Department of Mathematics, University of Utah, 115 John Widstoe Bldg., Salt Lake City, UT 84112. Tel.: 801-581-6089; Fax: 801-581-4148; E-mail: keener@math. utah. edu.

0006-3495/96/09/1335/11 $2.00

model is macroscopic but incorporates the appropriate cellular microscopic effects.

The outline of this paper is as follows. First, we describe the model in general terms and show how the model is capable of explaining global effects from local stimuli. If the tissue has equal anisotropy ratios, the model can be reduced to a monodomain model, for which simulations are relatively easy. We use numerical simulations to illustrate the usefulness of the model and to demonstrate a possible mechanism of defibrillation. These simulations elucidate the difference between successful and unsuccessful defibrillation. Our numerical experiments find substantial agreement in laboratory experiments (Chen et al., 1986; 1990; Witkowski et al., 1990). Our computations use simplified ionic current models and are not intended to be quantitative. However, the qualitative results are suggestive of how defibrillation might occur, or be unsuccessful, in realistic ionic models as well. Finally, in the Appendix, we give a derivation of the model equations, indicating differences between this model and the derivation and model of Neu and Krassowska (1993).

A MODEL FOR DIRECT ACTIVATION AND DEFIBRILLATION

For an understanding of how externally applied currents affect cardiac tissue, we need a model that distinguishes between the intracellular and extracellular spaces. Furthermore, to understand how inhomogeneities of resistance are responsible for the generation of transmembrane currents, we need to account for the small-scale resistive inhomogeneities of the medium. However, it is impractical, if not impossible, to create large-scale simulations of propagation (on the level of the intact heart or of large pieces of tissue) while keeping track of the fine-scale structure of the medium. Instead, we propose a new model that is resolved on the level of the macrostructure that nonetheless incorporates the effects of the cellular microstructure in an average sense. Models of this type are common in other fields such as material science, etc., and rely on the method of averaging or homogenization theory for their derivation. A derivation of the model from first principles is given in the Appendix to this paper.

Cardiac tissue is assumed to be a two-phase medium at the macroscopic level, with comingled intracellular and extracellular domains. At each point of the cardiac domain, denoted Ω, there are potentials ϕ_e and ϕ_i, the extracellular and intracellular potentials, respectively, and the transmembrane potential, $\phi = \phi_i - \phi_e$. These potentials drive currents,

$$i_e = -\sigma_e \nabla \phi_e, \qquad i_i = -\sigma_i \nabla \phi_i, \tag{1}$$

and a transmembrane current across the cell membrane dividing the two (comingled) regions. The conductivities of the two domains are represented by the conductivity tensors, σ_i and σ_e, which represent average, or effective, conductances of the media. Because current is conserved, Kirchhoff's laws imply that

$$\chi\left(C_m \frac{\partial \phi}{\partial t} + I_m\right) = \nabla \cdot (\sigma_i \nabla \phi_i) \tag{2}$$

$$\nabla \cdot (\sigma_i \nabla \phi_i + \sigma_e \nabla \phi_e) = 0 \tag{3}$$

The first of these equations implies that current can leave the intracellular space only as a transmembrane current, and that the transmembrane current has two components, namely the capacitive current and the ionic current I_m, and the second states that the total of intracellular and extracellular current $I_{tot} = -\sigma_i \nabla \phi_i - \sigma_e \nabla \phi_e$ is conserved, as there are no intracardiac current sources. In Eq. 2, C_m is the membrane capacitance, and χ is the ratio of cell surface to total volume.

The effect of the microstructure of the medium enters the governing equations through the ionic currents. For the standard bidomain model, the ionic currents are represented as

$$I_m = f(\phi, v), \tag{4}$$

where v represents recovery variables, gating variables, and the like. However, when the cellular microstructure is taken into account, the ionic current is modified to include dependence on the intracellular and extracellular electric fields, $\nabla \phi_i$ and $\nabla \phi_e$,

$$I_m = \bar{f}(\phi + \epsilon H(z, x), v), \tag{5}$$

where $H(z, x) = W_i(z) \cdot T^{-1} \nabla \phi_i - W_e(z) \cdot T^{-1} \nabla \phi_e$. Here x is the three-dimensional spatial Cartesian coordinate for the cardiac domain, and z is a "fast" three-dimensional variable, on the scale of cells $z = x/\epsilon$. The function $\bar{f}(u(z, x), v)$ is the average of f, averaged over the variable z over the surface of a single cell. The number ϵ is the ratio of cell length to longitudinal space constant $\epsilon = l/\Lambda$, and is generally small, on the order of 0.1–0.2. The vector valued functions $W_i(z)$ and $W_e(z)$ reflect the details of cellular structure, are periodic in z, and have zero mean value. The possibility of variable orientation of the cells is reflected in the x dependence of the rotation matrix $T(x)$, the rows of which are the normalized orthogonal axes of the cell.

It is useful to explain in words what all of this means. First, observe that if we ignore the function H, then the model is precisely the standard, and fully general, bidomain model. Therefore, the effects of large-scale resistive inhomogeneities such as unequal anisotropy ratios, fiber curvature, or rotation are incorporated in the model. The function H incorporates the effect of resistive inhomogeneities of the cellular scale, which are ignored in the standard bidomain model. Thus, the new model should give a better representation of reality than the fully general bidomain model.

The individual terms of H have the following interpretation. The functions W_i and W_e determine the relationship between currents and potentials at the cellular level. Because cells are not resistively homogeneous, the core con-

ductor assumption (that currents are uniformly distributed across a cross section of a cell) is certain to be incorrect. The functions W_i and W_e provide a leading order correction to the core conductor assumption, implicit in the standard bidomain model. These functions can be found explicitly as solutions of Laplace's equation with periodic boundary conditions (Eq. 40). Examples of the functions W_i and W_e were computed for hexagonal cells by Krassowska et al., (1990) and are well approximated by piecewise linear functions.

Multiplication with the matrix T^{-1} ensures that the assumed "standard cell" is placed in the tissue with the correct fiber orientation. The terms $\nabla\phi_i$ and $\nabla\phi_e$ represent the intracellular and extracellular electric fields.

The transmembrane potential comprises two components, a term ϕ, which is the local average transmembrane potential, and the term ϵH, which represents deviations of the transmembrane potential from its average value because of local inhomogeneities of resistance that generate local variations of transmembrane potential. The main point of Eq. 5 is that although the transmembrane current is not homogeneous across a cell membrane, it is sufficient to track the average transmembrane current. Deviations from this average are less significant.

Although this model is derived from first principles using generally accepted arguments, there is no rigorous mathematical theory to justify it or to estimate the conditions under which the model is valid. It is likely that the model is an improvement on the standard bidomain model, and that the correction terms are valid provided the spatial variation of the potentials is large compared to the length of cells. It is most likely to be incorrect if there are rapid spatial changes in resistivity, such as in the borders of infarcted tissue or in regions of high gap junctional resistance due to anoxia, for example.

The boundary conditions for the model are

$$\mathbf{n}\cdot\sigma_e\nabla\phi_e = \chi_c I(t), \qquad \mathbf{n}\cdot\sigma_i\nabla\phi_i = 0, \tag{6}$$

where $\mathbf{n}$ is the outward unit normal to the boundary, and χ_c is a *characteristic function* describing the geometrical features of the stimulus protocol. For example, if current is applied to the boundary through two pads of equal area, then $\chi_c = 1$ where there is inflow of current, and $\chi_c = -1$ where there is outflow of current, and is zero elsewhere. Because the net current input is zero it must be that

$$\int_{\partial\Omega} \chi_c \, dS = 0. \tag{7}$$

THE MECHANISM FOR DIRECT ACTIVATION AND DEFIBRILLATION

Because of local inhomogeneities of resistance, there are spatial variations in the transmembrane current and transmembrane potential at the spatial resolution of cells. The most important component of these currents is their spatial average. Because the ionic currents are nonlinear, this average can contribute to the overall ionic current in a significant way.

In normal circumstances when there is no applied current or when the applied current is not too large, the model (Eq. 5) reduces to the usual bidomain model because

$$I_m = \bar{f}(\phi + \epsilon H(z, x), v) = f(\phi, v) + O(\epsilon^2 H^2). \tag{8}$$

However, when the current input is large, say on the order of $1/\epsilon$, it can have an effect on the transmembrane current at every point in the domain.

Using a Taylor expansion, one can calculate directly that

$$I_m = \bar{f}(\phi + \epsilon H(z, x), v) = f(\phi, v) + \epsilon^2 J^2 \frac{\partial^2 f(\phi, v)}{\partial \phi^2} + O(\epsilon^3), \tag{9}$$

where $J^2 = \overline{H(z, x)^2}$. For example, for the cubic function $f(\phi, v) = \phi(\phi - 1)(\phi - a) + v$ (which is often used to describe excitable media and serves as a good paradigm), $(\partial^2 f(\phi, v))/\partial\phi^2 = 3\phi - a - 1$. For this example, we see that if ϕ is small, the fields $\nabla\phi_i$ and $\nabla\phi_e$ provide an inward (depolarizing) ionic current. On the other hand, if ϕ is larger than $(\alpha + 1)/3$, then the fields contribute a positive (outward) current and therefore are hyperpolarizing. Thus, the instantaneous state of a cell determines whether a shock is depolarizing or hyperpolarizing on a particular cell. In this simple cubic model, when a cell is excitable (recovered), a shock is depolarizing, but when a cell is excited, a shock is hyperpolarizing. This typifies the response for other ionic models, although the details are certainly different. The same effect is shown in Fig. 1 for the piecewise linear model that is used below for numerical computations. The impor-

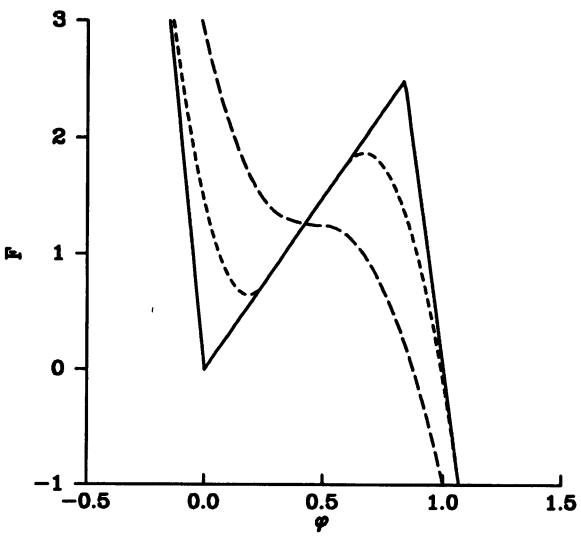

FIGURE 1 Plot of the averaged function $F(\phi, A)$ given by Eq. 24 for $A = 0$ (*solid line*), $A = 0.5$ (*short dashed curve*), and $A = 1.0$ (*long dashed curve*).

tant consequence here is that this depolarization of polarized cells and hyperpolarization of excited cells can be defibrillating, as we shall see below.

Direct activation (i.e., simultaneous activation of all tissue, not via a propagating action potential) of resting tissue ($\phi = 0$) occurs when the bias current is inward and large enough to overcome the tissue threshold. It is relatively easy to calculate this threshold for specific models (Keener, 1996).

Defibrillation is more complicated. During fibrillation, different regions of tissue are in different states, namely excited, refractory, or recovered. A stimulus has the effect of exciting any (hopefully all) recovered tissue. Because refractory tissue cannot be excited, after a defibrillatory shock all tissue is either excited or refractory. If there are no remaining recovered regions, action potential wavefronts stall and action potentials subsequently collapse as wave "backs" catch up with wavefronts, and the fibrillation is eliminated. If the stimulus is not large enough, some action potentials may collapse, while some may remain, allowing a fibrillatory state to be reestablished.

This scenario can be seen in one-dimensional simulations as in Keener (1996). Below we use numerical simulations to show how this mechanism works to defibrillate in two- and three-dimensional tissue as well.

For even larger amplitude stimuli, a different response is possible. At large currents, the averaged ionic current (Eq. 8) loses its nonlinear features and becomes monotonic in ϕ. However, with a monotonic ionic current, there is a unique, globally stable rest point and reentrant waves cannot persist. Thus, during the application of a large stimulus, the medium tends toward a uniform state which, after removal of the stimulus, returns to a uniform rest state.

SIMPLIFICATION OF THE MODEL

The distribution of currents during a defibrillatory shock is determined by tissue resistivities, including the anisotropy of the medium, the variation of the fiber orientation within the medium, and the inequality of the anisotropy ratios. Although all three of these are important, our model simplifies substantially if the medium has equal anisotropy ratios.

Suppose that the conductivity tensors are proportional with

$$\sigma_i = \alpha\sigma_e, \tag{10}$$

with α a constant. We try to represent the intracellular field $\nabla\phi_i$ as the sum of two contributions, one from the transmembrane potential and another to be determined, by writing

$$(\sigma_i + \sigma_e)\nabla\phi_i = \sigma_e\nabla\phi + (\sigma_i + \sigma_e)F. \tag{11}$$

Because $\sigma_i = \alpha\sigma_e$, it follows that F is the gradient of some function, $F = \nabla\psi$. Furthermore, it follows from Eq. 3 that ψ must satisfy

$$\nabla \cdot \sigma_e\nabla\psi = 0, \tag{12}$$

subject to boundary conditions

$$\mathbf{n} \cdot \sigma_e\nabla\psi = \chi_c\frac{I(t)}{1 + \alpha}. \tag{13}$$

It also follows that

$$(\sigma_i + \sigma_e)\nabla\phi_e = -\sigma_i\nabla\phi + (\sigma_i + \sigma_e)\nabla\psi. \tag{14}$$

Notice that the solution of the problem (Eq. 12) with boundary condition (Eq. 13) can be expressed as $\psi = I(t)/(1 + \alpha)\, G$, where G is a fundamental solution solving the time-independent problem

$$\nabla \cdot \sigma_e\nabla G = 0 \tag{15}$$

subject to boundary conditions

$$\mathbf{n} \cdot \sigma_e\nabla G = \chi_c. \tag{16}$$

The function G determines the potential distribution associated with an externally applied field.

Using G, we find that Eq. 2 becomes

$$\chi\left(C_m\frac{\partial\phi}{\partial t} + I_m\right) = \nabla \cdot \sigma\nabla\phi, \tag{17}$$

with ionic currents

$$I_m = \bar{f}\left(\phi + \frac{\epsilon}{1 + \alpha}(\nabla\phi \cdot T(W_i(z) + \alpha W_e(z)) + I(t)T(W_i(z) - W_e(z)) \cdot \nabla G),\, v\right), \tag{18}$$

and $\sigma = [\alpha/(1 + \alpha)]\sigma_e$ is the effective coupling coefficient, and the boundary conditions are

$$\mathbf{n} \cdot \sigma\nabla\phi = -\chi I(t)\frac{\alpha}{1 + \alpha}. \tag{19}$$

In Eq. 18, the transmembrane potential is modified by the addition of two terms. These are $[\epsilon/(1 + \alpha)]\nabla\phi \cdot T(W_i(z) + \alpha W_e(z))$, which is a self-induced correction term coming from the interplay between the transmembrane potential and the resistive inhomogeneities of the cell, and $I(t)T(W_i(z) - W_e(z)) \cdot \nabla G$, which, being proportional to the applied current $I(t)$, is the effect of an externally applied field on the transmembrane potential. In this model, because the ionic current I_m depends on both the gradient of the transmembrane potential $\nabla\phi$ and the externally applied current $I(t)$, even when there is no externally applied current, cellular inhomogeneities have an effect, albeit small, on action potential behavior.

The important observation here is that because we have assumed equal anisotropy ratios, this model is equivalent to a monodomain model in which the only unknown is the transmembrane potential ϕ. Once the time-independent function G is known, it can be used in the integration of ϕ with no additional computational complexity. Thus this model of direct activation and defibrillation has the same

computational demands as for propagation when there is no input current. Numerical simulation of the fully general model with unequal anisotropies requires the development of more sophisticated numerical schemes.

NUMERICAL SIMULATIONS

To illustrate the mechanism of defibrillation in this model, numerical simulations were performed using a standard two-variable model of an excitable medium. Parameters for the excitable dynamics were chosen so that spirals are not stable, but exhibit breakup and develop into "chaotic" reentrant patterns (Panfilov and Hogeweg, 1995), thereby giving a model of cardiac fibrillation. These dynamics provide an interesting test for the model because defibrillation cannot rely on any obvious regular patterns or symmetries.

For numerical computations, the tissue was assumed to be homogeneous and isotropic. We used FitzHugh-Nagumo-type dynamics, scaling space and time so that the governing equations (Eq. 17) are

$$\frac{\partial \phi}{\partial t} = \nabla^2 \phi - I_m(\phi, v) \tag{20}$$

$$\tau(\phi, v)\frac{\partial v}{\partial t} = (k\phi - v). \tag{21}$$

To include the effect of tissue resistivity, we approximated the cell structure functions $W_i(z)$ and $W_e(z)$ by piecewise linear functions of z, approximated the ionic current I_m by

$$I_m(\phi, v) = \bar{f}(\phi, A) = \int_{-1/2}^{1/2} f(\phi + Az)\, dz + v, \tag{22}$$

where $A = \epsilon R_g I(t)|\nabla G|$, and numerically tabulated $\bar{f}(\phi, A)$. The integration is over one unit of z because $z = x/\epsilon$ is the spatial variable on the scale of cells. That a linear approximation is reasonable follows from the calculations of W_i and W_e for hexagonal cells by Krassowska et al., (1990). From the one-dimensional problem (Keener, 1996), R_g is known to be a dimensionless number that represents the fraction of total resistance per unit length that is concentrated in the gap junctions. For this model, defibrillation thresholds are determined in terms of the parameter A.

We chose the nonlinear function f to be the piecewise linear function of "Pushchino kinetics" (Panfilov and Pertsov, 1984; Panfilov and Hogeweg, 1993):

$$f(\phi) = \begin{cases} C_1\phi & \text{when } \phi < \phi_1 \\ -C_2\phi + a & \text{when } \phi_1 < \phi < \phi_2, \\ C_3(\phi - 1) & \text{when } \phi > \phi_2 \end{cases} \tag{23}$$

where $\tau(\phi, v) = \tau_1$ when $\phi_1 < \phi < \phi_2$ and when $\phi < \phi_1$, $v > v_1$, $\tau(\phi, v) = \tau_2$, when $\phi > \phi_2$, and $\tau(\phi, v) = \tau_3$ when $\phi < \phi_1$ and $v < v_1$. The parameters determining the shape of the function $f(\phi)$ are $\phi_1 = 0.0026$, $\phi_2 = 0.837$, $v_1 = 1.8$, $C_1 = 20$, $C_2 = 3$, $C_3 = 15$, $a = 0.06$, and $k = 3$. With these parameter values the function $f(\phi)$ is continuous and N-shaped.

The function $f(\phi)$ determines fast processes such as the initiation of the action potential. The dynamics of the recovery variable v in Eq. 21 are determined by the function $\tau(\phi, v)$. In $\tau(\phi, v)$ the parameter τ_3 specifies the recovery time constant for small values of ϕ and v, and approximately determines the relative refractory period. Similarly, τ_1 specifies the recovery time constant for relatively large values of v and intermediate values of ϕ, approximately determining the action potential duration. For this computation, these parameters were chosen as $\tau_1 = 75$, $\tau_2 = 1$, and $\tau_3 = 2.75$.

The effect of a stimulating current is now reflected in the shape of the function

$$F(\phi, a) = \int_{-1/2}^{1/2} f(\phi + Az)\, dz. \tag{24}$$

This function is plotted in Fig. 1 for $A = 0$ (*solid curve*), $A = 0.5$ (*short dashed curve*), and $A = 1.0$ (*long dashed curve*). When there is no stimulating current, $A = 0$ and normal dynamics are followed. While the stimulating current is applied, the dynamics are temporarily changed in accordance with Fig. 1. For small A, the changes are only slight, but a resting excitable cell will be stimulated if A is sufficiently large for a sufficiently long period of time.

There are two ways that defibrillation can be accomplished. In the first (typified by the case $A = 0.5$ in Fig. 1), those regions of tissue that are partially recovered (ϕ near zero) receive a depolarizing stimulus, whereas those regions which are excited (with ϕ near 1) receive a hyperpolarizing stimulus, shortening the action potential duration. If this rearrangement of the action potential is sufficiently dramatic, it will be unable to propagate and will collapse.

For larger A (typified by $A = 1$ in Fig. 1) the dynamics are distorted, so that the medium is nonexcitable and reentrant patterns cannot persist. The effect of the applied current is to temporarily pull the flow toward a stable steady state. If A is sufficiently large, this temporary distortion of the flow is sufficient to eliminate reentrant patterns that may have previously existed.

To illustrate that the first of these indeed works, we performed numerical computations on two- and three-dimensional domains with a variety of preexisting patterns.

For numerical computations, we used explicit Euler time steps with homogeneous Neumann boundary conditions. Homogeneous boundary conditions were used to eliminate the large boundary effects that occur when large defibrillatory shocks are applied. At very large membrane potentials, cell properties change and the ionic currents are certainly modified in ways that are not adequately modeled by these dynamics.

Numerical computations in two dimensions were performed on a rectangular grid containing 200 × 200 elements and on a grid with 120 × 120 × 120 elements in

three dimensions. Numerical integration was performed with a space step $h_x = 0.6$ and a time step $h_t = 0.03$. The two-dimensional domain was chosen to be large enough that a spiral wave would consist of more than one full wrap. This demonstrates that the size and location of the spiral and the timing of the stimulus relative to the phase of the spiral do not affect the efficacy of the shock.

Defibrillation of a two-dimensional domain

At some time after initiating a wave pattern, a constant stimulus with a duration of 2 time units was applied. This is about 2.5 times the duration of the action potential upstroke for this model. The stimulus was deemed successful if after the stimulus ended, the wave pattern collapsed and the medium returned to rest. If the wave pattern persisted or another wave pattern was generated, the stimulus was deemed unsuccessful.

In the first series of computations we assumed that the stimulus was applied uniformly to pad electrodes applied to the entire left and right boundaries of the domain. This implies that $|\nabla G| =$ constant, so that the stimulating current and hence the number A is of uniform amplitude at all points of the medium.

We initiated a spiral wave using an artificially imposed wavebreak and allowed it to make four full rotations before applying a defibrillatory stimulus. At the time of stimulus, the spiral wave was still intact and had not deteriorated into chaotic reentry, although small nonuniformities of rotation were evident. Fig. 2 shows successful elimination of the spiral at $A = 0.98$. In Fig. 2 *a* we seen the spiral just before the stimulus is applied. The darkest shaded regions depict excited tissue, white regions are recovered and excitable, and grey regions (intermediate to the dark and light shades) are refractory. After application of the stimulus (Fig. 2 *b*), two significant events have occurred. Most important is that almost all previously relative refractory regions of the medium have been excited (shown as black), and the tails of the action potentials have been foreshortened, as there was forced recovery of tissue late in the action potential. Within short order, these distorted excited regions collapse (Fig. 2 *c*) and the medium subsequently returns to the rest state. In Fig. 2 *c* there is no excited tissue, although there is both refractory (*grey*) and recovered (*white*) tissue, in a spiral configuration that is the remnant of the recently eliminated propagating wavefront. The threshold in this case was $0.96 < A < 0.98$.

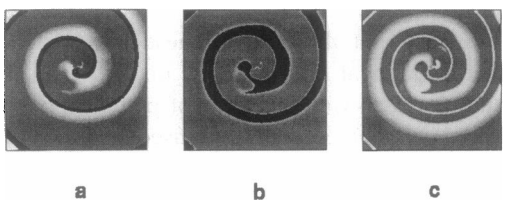

FIGURE 2 Successful defibrillation of a two-dimensional spiral wave in the model (Eqs. 20, 21, 23, and 24), with $A = 0.98$. The pictures are at times (*a*) $t = 0$ (before application of defibrillatory stimulus), (*b*) $t = 3.0$ (end of application of defibrillatory stimulus), (*c*) $t = 7.5$. Numerical integration was on a grid of 200 × 200 elements. The darkest areas represent the excited state of the tissue ($\phi > 0.6$), grey shows the region where $v > 1.8$ (close to the absolute refractory state), and intermediate shading from grey to white shows different levels of v, $0 < v < 1.8$ (estimate for the relative refractory period).

If the value of A was smaller than the threshold value, instead of removing the spiral, the stimulus initiated several spiral waves. An example of this behavior at $A = 0.9$ is shown in Fig. 3. The pattern just before the defibrillatory shock was the same as in Fig. 2 *a*, and the pattern of excitation just after the application of the stimulus was nearly identical to that in Fig. 2 *b*. However, at time $t = 7.5$, after most of the excitation has collapsed (Fig. 3 *a*), several islands of uncollapsed excitation remain, whereas in the previous case almost all excitation had collapsed by that time. These uncollapsed regions initiate several spiral waves (Fig. 3 *b*), which eventually develop into a complicated spatiotemporal pattern (Fig. 3 *c*).

To understand something about the relationship between excitability and the threshold for elimination of reentry, we repeated the above numerical simulation for eight different values of the parameter a. The parameter a appears in the definition of the function $f(\phi)$ in Eq. 23 and affects the excitability of the model, with less excitability for increasing a. Notice that for continuity, $\phi_1 = a/(C_1 + C_2)$.

The threshold A showed a (nearly linear) *decrease* as a function of the parameter a, with $A = 0.67$ at $a = 0.06$. The direct stimulus threshold is an increasing function of the parameter a because as excitability decreases, more current is required to stimulate a resting cell. However, when there is a reentrant pattern, none of the medium is fully recovered and at rest. In fact, at least in this model, reentrant patterns in less excitable media are easier to eliminate than in highly excitable media. This occurs in this model because the wavefronts in a reentrant pattern are more easily blocked in a less excitable medium than in a highly excitable medium. It is the nature of wavefronts in a reentrant pattern, not the nature of the medium at rest, that is the determining factor.

We do not claim that this is a general result, but it should be studied in more realistic models using parameters of physiological significance.

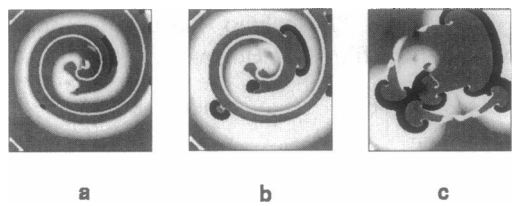

FIGURE 3 Unsuccessful defibrillation of a two-dimensional spiral wave in the model (Eqs. 20, 21, 23, and 24), $A = 0.90$. The pictures are at times (*a*) $t = 7.5$, (*b*) $t = 13.5$, (*c*) $t = 49.5$. The initial pattern, the moment of application, and duration of defibrillatory stimulus are the same as in Fig. 2. The grey scale coding is the same as in Fig. 2.

We also applied a defibrillatory stimulus to a turbulent wave pattern that was formed by a spiral break-up instability. Fig. 4 shows an example of successful defibrillation at $A = 0.86$. Fig. 4 *a* shows the initial pattern just before application of the stimulus, and Fig. 4 *b* shows the pattern just after application of the stimulus. In this case a few excitable spots remain in the medium at $t = 12$ (Fig. 4 *c*). However, there is not enough recovered space in the vicinity of these spots, and they eventually disappear. An example of unsuccessful defibrillation of this turbulent pattern (with $A = 0.84$) is shown in Fig. 5. The initial pattern just before application of the stimulus is the same as in Fig. 4 *a*, and Fig. 5 *a* shows the pattern just after termination of the stimulus, as in Fig. 4 *c*. After the stimulus and subsequent collapse of much of the excitation, one excited spot remains at the upper left corner of the medium, which eventually creates a double spiral, figure eight excitation pattern (Fig. 5 *c*). Similar patterns were found after unsuccessful defibrillation of the canine heart in laboratory experiments (Chen et al., 1990).

We compared the thresholds for defibrillation with a plane electrode to defibrillation thresholds with two point electrodes placed at the middle of the sides of opposite edges of the medium. With point electrodes the function $|\nabla G|$ is not constant, as it is for plane electrodes that cover the entire side, so the value $A = \epsilon R_g I(t)|\nabla G|$ is not constant. However, we report the threshold as a parameter A^* in units of total current flow through the boundary. That is, with $A^* = 1$, the total current flow through the stimulating electrode is the same as with a plate electrode with $A = 1$. Fig. 6 *f* shows level surfaces for the distribution of current $|\nabla G|$ using point electrodes.

Fig. 6 shows an example of successful defibrillation of the chaotic initial pattern in Fig. 4 *a* using point electrodes. The evolution subsequent to the stimulus shown in Fig. 6, *a–c*, is similar to that of Fig. 4, *a–c*, although there is one extra excited spot in the upper left corner of Fig. 6 *c*. However, because there is not sufficient recovered space around this spot, the excitation disappears (Fig. 6, *d* and *e*). The threshold for defibrillation in this case was $1.34 < A^* < 1.36$, higher than for plane electrodes, as expected.

Fig. 7 shows an example of unsuccessful defibrillation by point electrodes, using $A^* = 1.34$. Fig. 7 *a* shows the same amount of time as Fig. 6 *e*. Here a small excited spot survives and gives rise to a double spiral wave (Fig. 7 *b*), which later becomes a single spiral (Fig. 7 *c*).

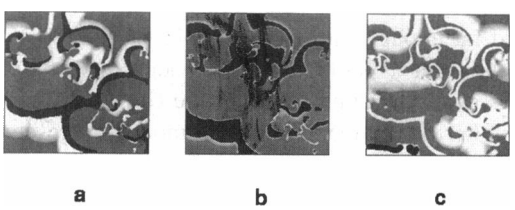

FIGURE 4 Successful defibrillation of two-dimensional turbulence in the model (Eqs. 20, 21, 23, and 24), $A = 0.86$. The pictures are at times (*a*) $t = 0$ (before application of defibrillatory stimulus), (*b*) $t = 3.0$ (end of application of defibrillatory stimulus), (*c*) $t = 12.0$. The grey scale coding is the same as in Fig. 2.

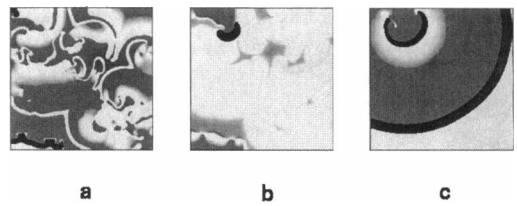

FIGURE 5 Unsuccessful defibrillation of two-dimensional turbulence in the model (Eqs. 20, 21, 23, and 24), $A = 0.84$. The pictures are at times (*a*) $t = 12.0$, (*b*) $t = 28.5$, (*c*) $t = 63$. The initial pattern, the moment of application and duration of defibrillatory stimulus are the same as in Fig. 4. The grey scale coding is the same as in Fig. 2.

Defibrillation of a three-dimensional domain

To defibrillate a three-dimensional domain, we applied a current generated by plane electrodes, giving a uniform current density throughout the medium. At the time of the stimulus, the wave pattern was that obtained after the turbulent break-up of a scroll wave, reported by Panfilov and Hogeweg (1995a,b).

Fig. 8 shows an example of successful defibrillation at $A = 0.85$. The pattern at the time of stimulus is shown in Fig. 8 *a*, and Fig. 8 *b* shows the pattern immediately after application of the stimulus. Later, the excited regions collapse (Fig. 8, *c* and *d*), and the medium returns to its rest state. The threshold for defibrillation in this case was $0.83 < A < 0.85$.

Unsuccessful defibrillation at $A = 0.8$ is shown in Fig. 9. Here the defibrillatory stimulus does not reset all of the medium, so that there are several excitable spots remaining

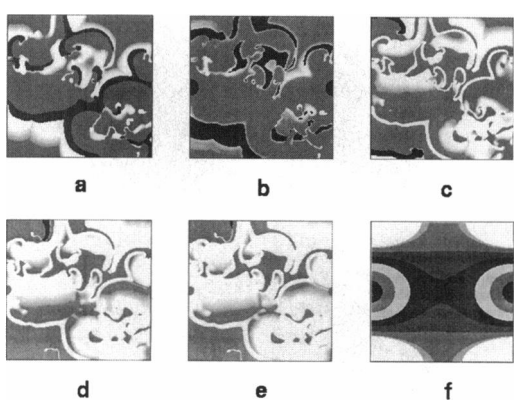

FIGURE 6 Successful defibrillation of two-dimensional turbulence in the model (Eqs. 20, 21, 23, and 24), by a point electrodes, $A = 1.36$. The pictures are at times (*a*) $t = 0$ (before application of defibrillatory stimulus), (*b*) $t = 3.0$ (end of application of defibrillatory stimulus), (*c*) $t = 12.0$, (*d*) $t = 16.5$, (*e*) $t = 18.0$. The grey scale coding of *a–e* is the same as in Fig. 2. (*f*). Distribution of the absolute value of current density in the medium. Different shades of grey correspond to different current levels.

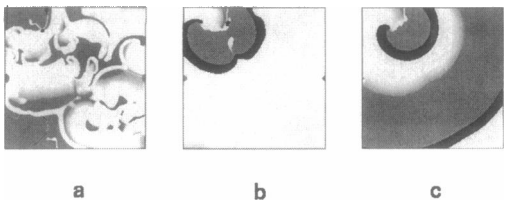

FIGURE 7 Unsuccessful defibrillation of two-dimensional turbulence in the model (Eqs. 20, 21, 23, and 24), by a point electrodes, $A = 1.34$. The pictures are at times (*a*) $t = 18.0$, (*b*) $t = 33.0$, (*c*) $t = 63.0$. The grey scale coding is the same as in Fig. 2.

(Fig. 9 *a*). These spots eventually develop into a three-dimensional turbulent pattern, similar to that which existed before the stimulus was applied (Fig. 9, *b–d*).

DISCUSSION

We found no major differences in defibrillation thresholds in two- and three-dimensional simulations, all being on the order of $A = 1$.

There were some minor differences in threshold for the elimination of a single spiral and defibrillation of a turbulent pattern ($0.96 < A < 0.98$ for a single spiral and $0.84 < A < 0.86$ for a two-dimensional turbulent pattern.) The reason for this difference relates to the details of the excitable gap in the two types of propagation, but we do not consider this difference to be of fundamental importance. The differences between the defibrillation thresholds of two-dimensional ($0.84 < A < 0.86$) and three-dimensional ($0.83 < A < 0.85$) turbulent patterns are negligible.

CONCLUSION

With this new model, a mechanism for defibrillation of cardiac tissue has been elucidated. Because of variations in resistance at the cellular level, an external stimulus generates hyperpolarizing and depolarizing transmembrane currents. Because the ionic currents depend nonlinearly on transmembrane potential, there is a net average effect that provides a depolarizing bias if the cell is sufficiently recovered. Even though the stimulus is applied locally, this depolarizing bias is transmitted to all excitable tissues by resistive inhomogeneities.

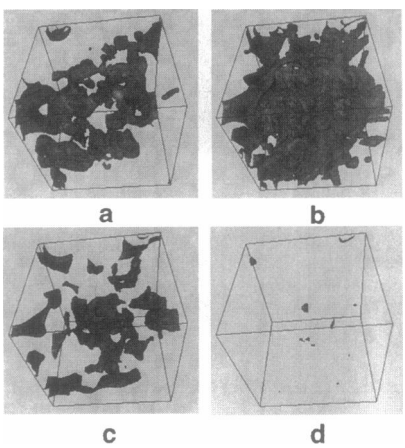

FIGURE 8 Successful defibrillation of three-dimensional turbulence in the model (Eqs. 20, 21, 23, and 24), $A = 0.85$. The pictures are at times (*a*) $t = 0$ (before application of defibrillatory stimulus), (*b*) $t = 3.0$ (end of application of defibrillatory stimulus), (*c*) $t = 6.0$, (*d*) $t = 7.5$. Numerical integration was on a grid of $120 \times 120 \times 120$ elements. The dark region depicts the excited region of the tissue ($e > 0.5$).

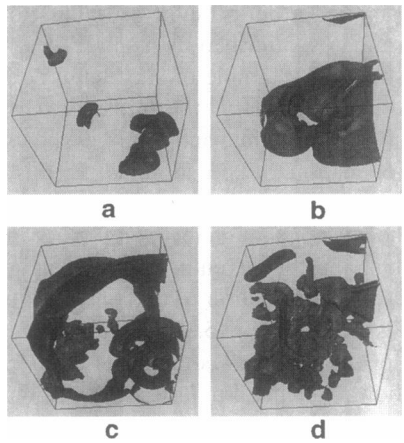

FIGURE 9 Unsuccessful defibrillation of three-dimensional turbulence in the model (Eqs. 20, 21, 23, and 24), $A = 0.80$. The pictures are at times (*a*) $t = 15$; (*b*) $t = 75$, (*c*) $t = 135$, (*d*) $t = 210$.

The sources of cellular resistivity include, but are not restricted to, gap junctional resistance. In this model, one can include the effects of any inhomogeneity of resistance in the intracellular or extracellular space. One can also incorporate effects of different cellular geometries and layout (for example, hexagonal grids). The assumption that the inhomogeneities are locally periodic is a first approximation of resistive properties of cardiac tissue. Our model does not assume a known applied electric field. Instead, the electric field that is generated by a shock is determined as part of the model from tissue conductivity properties.

The cellular dynamics that follow a defibrillatory shock are also elucidated by this model. A sufficiently large stimulus has the effect of activating all excitable tissue, eliminating the excitable gaps. Because the wavefront stalls, the reset action potential collapses as the back catches up with the front, thereby eventually returning the entire medium to rest. Defibrillation fails when the wavefront is not pushed forward far enough into the excitable gap. When this happens, the stall is only temporary and forward progress resumes as the medium ahead of the front recovers.

At higher amplitude stimuli, the model suggests another mechanism for defibrillation whereby the tissue is rendered spatially homogeneous by the shock and thereafter returns to rest. The numerical simulations reported here were not performed at these higher amplitudes.

Our results do not depend on the details of our model of ionic currents. The model used here is highly excitable, but the behavior and elimination of reentrant patterns depend

only secondarily on this detail. Furthermore, our paradigm for fibrillation is not important. In this model, spiral patterns degenerate spontaneously into erratic reentrant patterns resembling a fibrillatory state. There is no conclusive experimental evidence that this is the true mechanism of fibrillation, and it may be that the fibrillatory instability is caused by tissue inhomogeneities and structural alterations due to aging, hypertension, etc. The point of this model is to show how a defibrillatory stimulus can search out and destroy regions of excitability in a spatially contorted wavefront pattern, regardless of the mechanism of how that spatial contortion was created.

The defibrillation threshold was expressed in terms of the parameter $A = \epsilon R_g I|\nabla G|$, suggesting that there are a number of ways to modify the effect of a defibrillating shock. The most obvious way to exceed threshold is to increase the total current I. However, it is a prediction of this theory that the efficacy of defibrillation is increased by increasing the gap junctional resistance. This prediction is experimentally testable, using an agent that blocks gap junctions, such as heptanol.

Although this new model has many features to recommend it, and produces results that are in substantial agreement with many experimental observations, in this model there is no difference between the effects of monophasic and biphasic shocks. This is because, to leading order (with first-order averaging), the sign of the applied stimulus is lost. Experiments have clearly shown that biphasic shocks are substantially more effective than monophasic shocks (Zhou et al., 1993a,b), although there is as yet no theoretical explanation of this observation. The difference between our model and this well-established experimental fact may be the result of a number of simplifications and assumptions of the model. It could be that higher order effects not included in first-order averaging, resistive inhomogeneities on the scale of the tissue space constant, and local variations of the dynamics of recovery variables play important roles that are not captured in the present model.

APPENDIX: DERIVATION OF THE MODEL EQUATIONS

The homogenization of a periodic conductive domain

The purpose of this appendix is to derive the model equations (Eqs. 2, 3, 5) for cardiac tissue using homogenization (averaging) techniques. The derivation will consist of two parts. In the first we solve a canonical problem to find the potential on a domain with periodic microstructure, and then we use the solution of this equation to find the equations governing transmembrane potentials.

The technique we use here is closely related to that of Neu and Krassowska (1993), with some clarifications and corrections, although the resulting model differs in important ways (described below).

We assume that cardiac tissue is separated into two continuous domains by cell membrane. An individual cell is some small periodic subunit Ω contained in a small rectangular box. The rectangular box is divided into intracellular space and extracellular space, separated by cell membrane. The cells are connected to each other at the sides of the boxes through gap junctions, which are simply parts of the box wall that are contiguous with intracellular space. Thus, the boundary of the cellular subunit $\partial\Omega_b$ is composed of two components, cell membrane $\partial\Omega_m$ and sides of the box $\partial\Omega_b$ at the junctions.

It is permissible to take the periodic subunit to be a small collection of cells, if, for example, one wishes to determine the effects of hexagonal packing of cells rather than rectangular packing.

For this first computation, we do not need to distinguish between intracellular and extracellular space, as the analysis is the same for both. In either of these spaces, currents are driven by a potential and satisfy Ohm's law, $r_c i = -\nabla\phi$, where r_c is the cytoplasmic resistance (a scalar). On the interior of the region, current is conserved, so that

$$\nabla^2\phi = 0. \tag{25}$$

Current enters the domain only across boundaries, according to

$$\mathbf{n}\cdot\frac{1}{r_c}\nabla\phi = I_m, \tag{26}$$

applied in the cell membrane, denoted $\partial\Omega_m$, and where $\mathbf{n}$ is the outward unit normal to the membrane boundary.

Suppose that x is the original three-dimensional Cartesian coordinate space. To allow for a variable fiber structure we will assume that the orientation of the rectangular boxes is slowly varying (hence they are not exactly rectangular, but are close enough), and that the axes of the rectangular cellular boxes form a natural "fiber" coordinate system. At each point in space the orientation of the rectangular box is determined by three orthogonal tangent vectors, forming the rows of the matrix $T(x)$. Then the fiber coordinate system is related to the original Cartesian coordinate system through

$$y = Y(x) = \int T(x)\,dx, \tag{27}$$

so that

$$\nabla_x = T(x)\nabla_y, \tag{28}$$

and in the y coordinate system,

$$\nabla^2\phi = \nabla_y^2\phi + \kappa\cdot\nabla_y\phi. \tag{29}$$

The vector κ is the curvature vector, the components of which are the mean curvatures of the coordinate level surfaces. If the components of the matrix T are given by T_{ij}, then the coordinates of κ are $\kappa_j = t_{ik}\,\partial t_{ij}/\partial x_k$.

Now we take into account that the boundary of the cells is varying rapidly on the scale of the fiber coordinate system, and so introduce the "fast" variable $z = y/\epsilon$, where ϵ is the small dimensionless parameter $\epsilon = l/\Lambda$, l is the longitudinal length of the cell, and Λ is the natural length scale along fibers. We assume that κ is a function solely of y, because variations of fiber direction are not noticeable at the cellular level.

Here we have a problem on two scales that we will solve by making the usual "two-variable" assumption. That is, we treat y and z as independent variables, and following the chain rule, write

$$\nabla_y \to \nabla_y + \frac{1}{\epsilon}\nabla_z. \tag{30}$$

In terms of the two variables y and z, problem 25 becomes

$$\frac{1}{\epsilon^2}\nabla_z^2\phi + \frac{2}{\epsilon}\nabla_z\cdot\nabla_y\phi + \nabla_y^2\phi + \frac{1}{\epsilon}\kappa\cdot\nabla_z\phi + \kappa\cdot\nabla_y\phi = 0, \tag{31}$$

subject to the boundary conditions

$$\frac{1}{r_c}\mathbf{n}\cdot\left(\frac{1}{\epsilon}\nabla_z\phi + \nabla_y\phi\right) = I_m(y, z) \tag{32}$$

on $\partial\Omega_m$ in z. We seek a solution that is periodic in the variable z.

The solution of this expanded partial differential equation is solved using the power series in ϵ:

$$\phi(y, z) = \frac{1}{\epsilon}\Phi(y) + \phi_0(y, z) + \epsilon\phi_1(y, z) + \epsilon^2\phi_2(y, z) + O(\epsilon^3), \tag{33}$$

where all functions are taken to be periodic in z. We create a hierarchy of equations to be solved by substituting the assumed solution form 33 into the governing Eq. 31, and collecting like powers of ϵ, with the result that

$$\nabla_z^2\phi_0 = 0 \tag{34}$$

$$\nabla_z \cdot (\nabla_z\phi_1 + \nabla_y\phi_0) + (\nabla_y + \kappa) \cdot (\nabla_z\phi_0 + \nabla_y\Phi) = 0. \tag{35}$$

In a similar fashion, we find a hierarchy of boundary conditions

$$\frac{1}{r_c}\mathbf{n} \cdot (\nabla_z\phi_0 + \nabla_y\Phi) = 0 \tag{36}$$

$$\frac{1}{r_c}\mathbf{n} \cdot (\nabla_z\phi_1 + \nabla_y\phi_0) = I_m(y, z) \tag{37}$$

applied on $\partial\Omega_m$, the membrane wall.

Now we solve this hierarchy of equations, one at a time. At this stage Φ is not known. However, ϕ_0 must be of the form

$$\phi_0(y, z) = W(z) \cdot \nabla_y\Phi(y) + \Phi_0(y). \tag{38}$$

Here, $W(z)$ is a fundamental solution vector, periodic in z with zero surface average value $\int_{\partial\Omega_m} W(z)\, dS_z = 0$, and satisfies the vector partial differential equation

$$\nabla_z^2 W(z) = 0, \tag{39}$$

subject to the boundary condition

$$\mathbf{n} \cdot (\nabla_z W(z) + I) = 0 \tag{40}$$

on $\partial\Omega_m$, the membrane wall. Here I is the identity matrix. This fundamental problem separates into three independent problems for the three components of $W(z)$. Because the governing problem is linear, we can take $\Phi_0(y) = 0$ without loss of generality.

According to the divergence theorem, for any diffentiable vector valued function $f(z)$,

$$\int_\Omega \nabla \cdot f\, dV_z = \int_{\partial\Omega} \mathbf{n} \cdot f\, dS_z. \tag{41}$$

Furthermore, if $f(z)$ is periodic in z, then

$$\int_{\partial\Omega_b} \mathbf{n} \cdot f\, dS_z = 0. \tag{42}$$

It follows that

$$\int_\Omega \nabla_z \cdot (\nabla_z\phi_1 + \nabla_y\phi_0)\, dV_z = \int_{\partial\Omega_m} \mathbf{n} \cdot (\nabla_z\phi_1 + \nabla_y\phi_0)\, dS_z. \tag{43}$$

Thus, a necessary condition for Eq. 35 to have a solution is that

$$\int_\Omega \frac{1}{r_c}(\nabla_y + \kappa) \cdot (\nabla_z\phi_0 + \nabla_y\Phi)\, dV_z = -\int_{\partial\Omega_m} I_m(y, z)\, dS_z. \tag{44}$$

Substituting the solution (Eq. 38) into the integral condition (Eq. 44), we find the condition

$$(\nabla_y + \kappa) \cdot \left(\frac{1}{r_c}\int_\Omega (\nabla_z W(z) + I) dV_z\right)\nabla_y\Phi = -\int_{\partial\Omega_m} I_m(y, z)\, dS_z. \tag{45}$$

We identify the average conductivity tensor (the inverse of the average resistance per unit length) as

$$\sum = \frac{\epsilon}{r_c V}\int_\Omega (\nabla_z W(z) + I)\, dV_z, \tag{46}$$

where V is the volume of the rectangular box containing the cell. Even though Σ is multiplied by the scalar ϵ, it is not a small quantity. This is because the conductance of an individual cell Σ/ϵ is large. The quantity Σ is an experimentally measured quantity.

Now we write Eq. 45 in terms of the original Cartesian coordinate variable x as

$$\nabla \cdot (\sigma\nabla\Phi) = -\frac{\epsilon}{V}\int_{\partial\Omega_m} I_m(y, z)\, dS_z, \tag{47}$$

where $\sigma(x) = T\Sigma T^{-1}$.

In summary, we have found ϕ to be of the form

$$\phi = \frac{1}{\epsilon}\Phi(x) + W(z) \cdot T^{-1}\nabla_x\Phi(x) + O(\epsilon\Phi), \tag{48}$$

where Φ satisfies the equation

$$\nabla \cdot (\sigma\nabla\Phi) = -\frac{\epsilon}{V}\int_{\partial\Omega_m} I_m(y, z)\, dS_z. \tag{49}$$

The bidomain equations

To make use of this solution for cardiac tissue, we define the potentials of the intracellular and extracellular domains as ϕ_i and ϕ_e, respectively. Then the transmembrane potential is the difference between the two potentials across the membrane

$$\phi = (\phi_i - \phi_e)|_{\partial\Omega_m}. \tag{50}$$

At each point of the cell membrane the outward transmembrane current is given by

$$I_m = C_m\frac{d\phi}{dt} + \frac{1}{R_m}F_m(\phi), \tag{51}$$

where C_m is the membrane capacitance and F_m/R_m represents the transmembrane ionic current. The parameter R_m is the membrane resistance.

From our foregoing analysis, we know that the potentials have average components, say ψ_i and ψ_e, and fine-scale variations from these averages, given by

$$\phi_i = \psi_i(x) + \epsilon W_i(z) \cdot T^{-1}\nabla\psi_i(x) + O(\epsilon^2\psi_i) \quad (52)$$

$$\phi_e = \psi_e(x) + \epsilon W_e(x) \cdot T^{-1}\nabla\psi_e(x) + O(\epsilon^2\psi_e), \quad (53)$$

and that $\psi_i(x)$ and $\psi_e(x)$ satisfy the equation

$$\nabla\cdot(\sigma_i\nabla\psi_i) = -\nabla\cdot(\sigma_e\nabla\psi_e) = \frac{1}{V}\int_{\partial\Omega_m} I_m(x, z)\, dS_z, \quad (54)$$

where I_m is the transmembrane current (positive outward). We calculate that (recall that $\int_{\partial\Omega_m} W_i\, dS_z = \int_{\partial\Omega_m} W_e\, dS_z = 0$)

$$\int_{\partial\Omega_m} I_m(x, z)\, dS_z \quad (55)$$

$$= C_m S_m \frac{\partial\psi}{\partial t} + \frac{1}{R_m}\int_{\partial\Omega_m} F_m(\psi + \epsilon H(z, x))\, dS_z,$$

where

$$H(z, x) = W_i(z)\cdot T^{-1}\nabla\psi_i(x) - W_e(z)\cdot T^{-1}\nabla\psi_e(x) \quad (56)$$

$$\psi = \psi_i - \psi_e. \quad (57)$$

It follows that

$$\nabla\cdot(\sigma_i\nabla\psi_i) = -\nabla\cdot(\sigma_e\nabla\psi_e) \quad (58)$$

$$= \chi\left(C_m\frac{\partial\psi}{\partial t} + \frac{1}{R_m}\frac{1}{S_m}\int_{\partial\Omega_m} F_m(\psi + \epsilon H(z, x))\, dS_z\right).$$

The parameter $\chi = S_m/V$ is the ratio of cell surface area per unit volume. Eq. 58 is the model used in this paper.

The derivation and model given here are similar to those given by Neu and Krassowska (1993), although they differ in important ways. The primary difference is that in Neu and Krassowska (1993), the function $H(z, x)$ in Eq. 56 is

$$H(z, x) = E\cdot(W_i(z) - W_e(z)), \quad (59)$$

where E is the externally applied electric field. Two observations are immediate. First, the electric field E is not determined by the model but must be supplied by some other means, and the effects of anisotropy or fiber orientation on E are not known. Second, the effects of this field on intracellular space and extracellular space are presumed to be identical. That is, there is no accounting for possible differences between the intracellular field and the extracellular field, because the two are assumed to be equal. This is not likely to be correct in any realistic tissue model.

This error arises in the derivation of Neu and Krassowska (1993) because of an oversight, wherein Eq. 26 is not satisfied to leading order. These differences play no role in normal situations of action potential propagation or with current stimuli of modest amplitudes. The differences become significant, however, when stimulating currents and fields are large, as during defibrillatory shocks, the situation examined in this paper.

With the assumption of equal anisotropy ratios, the model presented here simplifies to a monodomain model for which numerical simulations are straightforward. However, this assumption is by no means required of the model. Simulations incorporating the effects of unequal anisotropy ratios, variable fiber orientation, and local resistive inhomogeneities will be the topics of forthcoming work.

This research was supported in part by National Science Foundation grant DMS 9303502.

REFERENCES

Chen, P., N. Shibata, P. Wolf, E. Dixon, N. Danieley, M. Swinney, W. Smith, and R. Ideker. 1986. Epicardial activation during successful and unsuccessful ventricular defibrillation in open chest dogs. *Cardiovasc. Rev. Rep.* 7:625–648.

Chen, P., P. Wolf, S. Melnick, N. Danieley, W. Smith, and R. Ideker. 1990. Comparison of activation during ventricular fibrillation and following unsuccessful defibrillation shocks in open-chest dogs. *Circ. Res.* 66: 1544–1560.

Keener, J. P. 1996. Direct activation and defibrillation of cardiac tissue, *J. Theor. Biol.* 178:313–324.

Knisely, S. B., T. F. Blitchington, B. C. Hill, A. O. Grant, W. M. Smith, T. C. Pilkington, and R. E. Ideker. 1993. Optical measurements of transmembrane potential changes during electrical field stimulation of ventricular cells. *Circ. Res.* 72:255–270.

Krassowska, W., D. W. Frazier, T. C. Pilkington, and R. E. Ideker. 1990. Potential distribution in three-dimensional periodic myocardium. II. Application to extracellular stimulation. *IEEE Trans. Biomed. Eng.* 37:267–284.

Krassowska, W., and J. C. Neu. 1994. Response of a single cell to an external electric field. *Biophys. J.* 66:1768–1776.

Krassowska, W., T. C. Pilkington, and R. E. Ideker. 1987. Periodic conductivity as a mechanism for cardiac stimulation and defibrillation. *IEEE Trans. Biomed. Eng.* 34:555–559.

LeGrice, I. J., B. H. Smaill, L. Z. Chai, S. G. Edgar, J. B. Gavin, and P. J. Hunter. 1995. Laminar structure of the heart: ventricular myocyte arrangement and connective tissue architecture in the dog. *Am. J. Physiol.* 269:H571–H582.

Neu, J. C., and W. Krassowska. 1993. Homogenization of syncytial tissues. *Crit. Rev. Biomed. Eng.* 21:137–199.

Panfilov, A., and P. Hogeweg. 1993. Spiral break-up in a modified FitzHugh-Nagumo model. *Phys. Lett. A.* 176:295–299.

Panfilov, A. V., and P. Hogeweg. 1995. Spiral break-up in a modified Fitzhugh-Nagumo model. *Phys. Lett. A.* 176:295–299.

Panfilov, A., and P. Hogeweg. 1995. Turbulence in a three-dimensional excitable media. *Science.* 270:1223–1224.

Panfilov, A., and A. Pertsov. 1984. Vortex ring in three-dimensional active medium in reaction-diffusion system. (in Russian) *Dokl. Akad. Nauk SSSR.* 274:1500–1503.

Plonsey, R., R. C. Barr, and F. X. Witkowski. 1991. One-dimensional model of cardiac defibrillation. *Med. Biol. Eng. Comput.* 29:465–469.

Pumir, A., and V. I. Krinsky. 1996. How does an electric field defibrillate cardiac muscle? *Phys. D.* 91:205–219.

Witkowski, F. X., P. A. Penkoske, and R. Plonsey. 1990. Mechanism of cardiac defibrillation in open-chest dogs with unipolar dc-coupled simultaneous activation and shock potential recordings. *Circulation.* 82: 244–260.

Zhou, X., J. P. Daubert, P. D. Wolf, W. E. Smith, and R. E. Ideker. 1993a. Epicardial mapping of ventricular defibrillation with monophasic and biphasic shocks in dogs. *Circ. Res.* 72:145–160.

Zhou, X., R. E. Ideker, T. F. Blitchington, W. E. Smith, and S. B. Knisely. 1995. Optical transmembrane potential measurements during defibrillation-strength shocks in perfused rabbit hearts. *Circ. Res.* 77:593–602.

Zhou, X., P. D. Wolf, D. L. Rollins, Y. Afework, W. E. Smith, and R. E. Ideker. 1993b. Effects of monophasic and biphasic shocks on action potentials during ventricular fibrillation in dogs. *Circ. Res.* 73:325–334.